Analysis of brain network dynamics estimated from fMRI data: A new framework based on communicability and flow

Matthieu Gilson[a,1], Nikos E. Kouvaris[b], Gustavo Deco[a,c], Jean-François Mangin[d], Cyril Poupon[d], Sandrine Lefranc[d], Denis Rivière[d], Gorka Zamora-López[a]

[a]Center for Brain and Cognition, Computational Neuroscience Group, Department of Information and Communication Technologies, Universitat Pompeu Fabra, Carrer de Ramon Trias Fargas 25-27, Barcelona 08005, Spain
[b]Namur Institute for Complex Systems (naXys), Department of Mathematics, University of Namur, Rempart de la Vierge 8, B 5000 Namur, Belgium
[c]Institució Catalana de la Recerca i Estudis Avançats (ICREA), Universitat Pompeu Fabra, Passeig Lluís Companys 23, Barcelona, 08010, Spain
[d]Institut d'Imagerie BioMédicale, Neurospin, Commissariat à l'Énergie Atomique, F-91191 Gif sur Yvette, France

Abstract

Neuroimaging techniques such as MRI have been widely used to explore the associations between brain areas. Structural connectivity (SC) captures the anatomical pathways across the brain and functional connectivity (FC) measures the correlation between the activity of brain regions. These connectivity measures have been much studied using network theory in order to uncover the distributed organization of brain structures, in particular FC for task-specific brain communication. However, the application of network theory to study FC matrices is often "static" despite the dynamic nature of time series obtained from fMRI. The present study aims to overcome this limitation by introducing a network-oriented analysis applied to whole-brain effective connectivity (EC) useful to interpret the brain dynamics. Technically, we tune a multivariate Ornstein-Uhlenbeck process to reproduce the statistics of the whole-brain resting-state fMRI signals, which provides estimates for EC as well as input properties (similar to local excitabilities). The network analysis is then based on the network response (or Green function) that describes the interactions between nodes across time for the estimated dynamics. This model-based approach provides time-dependent graph-like descriptors —communicability and flow— that characterize the roles that either nodes or connections play in the propagation of activity within the network. They can be used at both global and local levels, and also enables the comparison of estimates from real data with surrogates (e.g., random network or ring lattice). In contrast to classical graph approaches to study SC or FC, our framework stresses the importance of taking the temporal aspect of fMRI signals into account. Our results show a merging of functional communities over time (in which input properties play a role), moving from segregated to global integration of the network activity. Our formalism sets a solid ground for the analysis and interpretation of fMRI data, including task-evoked activity.

1. Introduction

The study of the brain network has attracted much attention in recent years as a collective attempt to understand how distributed and flexible cognitive functions operate. A large body of data-driven studies has focused on the interpretation of brain connectivity measured by structural and functional magnetic resonance imaging (sMRI and fMRI, respectively); for a review see [1]. A particular focus [2] has been on the relationship between the structural connectivity (SC), which is the architecture of connections between brain regions, and

---

[1]Corresponding author: matthieu.gilson@upf.edu; Universitat Pompeu Fabra, C/ Ramon de Trias Fargas, 25-27, Barcelona 08005, Spain

functional connectivity (FC), the correlation structure of the observed activity. Initially, SC and FC were investigated using statistical descriptors designed for graphs such as the degree distribution and clustering coefficient [3, 4, 5]. Brain areas can then be characterized —often in an off-the-shelf manner— such as highly connected hubs that are hypothesized to centralize information distributed across the brain. Following, the concept of communicability was proposed as a model of interactions in a graph to link the network structure to the pairwise functional associations of nodes [6]. It has then been used to derive measures that describe the roles for nodes in networks [7] and to define a new version of centrality in graphs [8, 9]. In the context of neuroimaging, graph communicability has been applied to evaluate the contribution of SC topology in generating FC [10]. The SC topology explains part of the FC structure, but this type of modeling is limited for explaining the time-series nature of the fMRI measurements.

In this context the present study aims to describe the fMRI-related functional associations between the nodes in the brain network, also known as regions of interest (ROIs), while properly taking time into account. We follow recent works that employed dynamic models of the brain activity to link SC and FC [11]. A great variety of network designs has been explored to combine experimental data in various levels of detail [12, 13, 14, 15, 16]. These dynamic models typically involve a connectivity matrix that describes how the activity propagates in the network. This should be contrasted with another active line of research focusing on the 'dynamic FC' that relies on sliding time windows to capture the statistical (functional) dependences between ROIs on the timescale of a minute [17]. The statistical analysis of these successive connectivity measures can lead to the definition of "states" for the whole network or ROIs [18, 19, 20]. Only after, the transitions between the obtained states are examined, for instance using hidden Markov models (HMMs) that generate dynamic FC in each window [21, 22]. A common aspect for the second type of studies is the representation of BOLD time series as independent "static" snapshots corrupted by noise, without considering the transition between successive BOLD activities. Instead, we aim to address this limitation by providing a network-oriented analysis that takes into account the propagation nature of BOLD signals.

Definition of integration measures have been proposed to quantify how nodes in the network exchange information at the scale of the whole network, thus building a global workspace [23, 24]. Previously-proposed definitions of integration have focused the similarity as measured using mutual information or the cross-correlation between the observed activity of subgroups of nodes in the network [25, 26, 27]. The resulting 'network complexity' of the network activity reflects the superposed contribution of hubs and network motifs such as modules [28]. Moreover, when network analysis is used with generative models to interpret the collective pattern of interactions between ROIs or quantify integration, it is most often applied on the model activity, such as the model dynamic FC to take time into account [29, 30, 31]. Therefore, it can be argued that these previously-proposed measures for integration focus on the observed or generated activity rather than their causes. To explore this point we will compare network analyses based on the ROI correlation pattern and based on measures of the causal interactions between ROIs in a model.

Here we present a model-based approach that focuses on the effective connectivity (EC) instead of the FC or SC as a basis for network analysis. It aims to incorporate time in the network analysis by accounting for the propagation nature of the BOLD dynamics. Our framework relies on a dynamic model —multivariate Ornstein-Uhlenbeck (MOU) process— fitted to whole-brain BOLD signals, where EC measures the causal interactions between ROIs and relates to the "generator" of the model activity [14, 32]. The relationship with other network models such as dynamic causal model [33] will be discussed later. The mathematical tractability of the MOU allows for the interpretation of the model estimates –in particular EC— in terms of interaction over time between the brain regions [34]. This provides a consistent analysis based on the same network dynamics from the estimation to the interpretation, in contrast to previously-proposed formalisms that applied "artificial" dynamics on static networks obtained from neuroimaging data [35, 36, 37, 6, 7]. The rationale is the following: The dynamic model is an assumption (a prior) about the spatio-temporal structure of the

empirical time series and the estimation is a "projection" of the fMRI data on the space of model parameters. The tuned dynamic model can then be used to examine the interactions between the brain regions.

After recapitulating in Methods important points about the model optimization to fMRI data [14], we present the formalism to analyze complex network dynamics with linear coupling [34]. It is based on two core graph-like measures for the interactions between brain regions: *dynamic communicability* and *flow*, which depend over time and serve as the basis for multivariate descriptors. We illustrate the framework using resting-state fMRI and diffusion MRI of the ARCHI database acquired by the European project Connect [38, 39] and freely available from the HBP Neuroinformatics platform. In particular, we show how communicability provides a finer and more general description of the network dynamics —by capturing the propagation of the BOLD signals throughout the whole network via EC— than classical analysis based on FC or SC. At the end, we perform community analysis and show how the network displays integration of information, first locally and then globally.

2. Methods

2.1. Acquisition of resting-state fMRI time series and structural connectomes

The analyses were applied to the ARCHI database [38, 39] composed of 79 subjects (32 females, mean age 23.65 years, SD=5.16) with high quality T1-weighted images and diffusion data, acquired on a Magnetom TimTrio 3T MRI System (Siemens Healthcare, Erlangen, Germany).

Resting state fMRI data were acquired using the following parameters: GRE EPI sequence, isotropic spatial resolution $3.0 \times 3.0 \times 3.0$ mm3, 40 slices, field of view 192 mm, phase FOV 100%, slice thickness 3.0 mm, TE = 30 ms, TR = 2400 ms, flip angle FA = $81°$, matrix 64×64, read bandwidth RBW = 2442 Hz/pixel, echo spacing ES = 0.47 ms, 1 excitation, interlaced multislice, EPI factor 64, total scan time 9 min 47 s.

The MRI protocol used in this study included anatomical T1-weighted images at one millimeter isotropic spatial resolution, a B0 fieldmap to correct for susceptibility artifacts, and a high angular resolution diffusion imaging (HARDI) dataset along 60 optimized directions at a b value of 1500 s/mm2 with an isotropic spatial resolution of $1.7 \times 1.7 \times 1.7$ mm3. The imaging parameters were as follows: T1-weighted data: 160 slices, FOV 256 mm, Phase FOV 93.8%, slice thickness, 1.1 mm, TE/TR = 2.98/2300 ms, TI = 900 ms, FA = $9°$, matrix 256×240, RBW=240 Hz/pixel; diffusion data: 70 slices, field of view 220 mm, phase FOV 100%, slice thickness 1.7 mm, TE = 93 ms, TR=14 s, flip angle FA = $90°$, matrix 128×128, read bandwidth RBW = 1502 Hz/pixel, echo spacing ES = 0.75 ms, 1 excitation, partial Fourier factor PF = 6/8, parallel acceleration factor GRAPPA = 2, total scan time 16 min 46 s.

Both structural and functional MRI data were processed using Freesurfer 5.3 software [40], which performed cortical tissue (gray and white matters) segmentation, and surface mesh building for both pial interface and grey/white interface of each hemisphere. Surface alignment was performed to an inter-subject template, allowing the projection of atlases on the anatomical meshes, involving the Freesurfer Desikan atlas [41] and the surface projection of the AAL atlas [42]. The fMRI activity was obtained by averaging the projected BOLD signals over each ROI of the AAL atlas, see Table 1 below.

Individual SC matrices were built using Diffusion weight imaging (DWI) following the processing steps of the Connectomist-2.0 software [43]: artifact correction, geometrical distortion correction, analytical Q-ball model [44], streamline probabilistic fiber tracking inside an improved T1-based brain mask [45] using 27 seeds per voxel at the T1 image resolution and propagation step size of 0.4 mm. Unreliable short fibers under 30 mm were removed, then region-to-region SC matrices could be built by counting fibers connecting regions of a given atlas [46]. From the individual SC matrices, we calculate a generic SC matrix by averaging over all subjects.

Table 1: List of the 43 ROI labels for the AAL parcellation [42]. The order of Fig. 3a, from top to bottom. The parcellation has 1 such ROI for each hemisphere.

Label	Description
ITMP	inferior temporal cortex
TPM	middle temporal pole
MTMP	middle temporal cortex
TPS	superior temporal pole
STMP	superior temporal cortex
HSCHL	Heschl gyrus
PARAC	paracentral lobule
POSTC	postcentral gyrus
PREC	precentral gyrus
PCUN	precuneus
ANG	angular gyrus
SMAR	supramarginal cortex
IPAR	inferior parietal cortex
SPAR	superior parietal gyrus
FUS	fusiform gyrus
IOCC	inferior occipital cortex
MOCC	middle occipital cortex
SOCC	superior occipital cortex
LING	lingual gyrus
CUN	cuneus
CALC	calcarine gyrus
INS	insula
AMYG	amygdala
PARH	parahippocampal cortex
HIP	hippocampus
CPOST	cingulate posterior cortex
CMID	cingulate middle cortex
CANT	cingulate anterior cortex
OFCL	orbitofrontal cortex lateral
OFCP	orbitofrontal cortex posterior
OFCA	orbitofrontal cortex anterior
OFCM	orbitofrontal cortex medial
REC	rectus gyrus
ORBM	orbitrofrontal medial cortex
SFM	frontal superior medial
SMA	superior motor area
ROL	rolandic opercularis
ORBI	pars orbitalis
PTRI	pars triangularis
OPER	pars opercularis
MF	middle frontal cortex
SF	superior frontal cortex

2.2. Noise-diffusion model to interpret whole-brain fMRI data

The network dynamic model [14, 32] combines two key aspects:

- A whole-brain approach [12] is necessary to properly take into account the distributed nature of information conveyed by BOLD signals, as was experimentally observed for high-level cognition [47] or neuropathologies [48].

- In the model the directional connections between brain regions describe causal interactions, which corresponds to the concept of EC that was developed along with the dynamic causal model [33]. Here the EC weights are optimized such that the model reproduces the spatio-temporal structure of the BOLD signals, which was shown to convey information about the behavior condition of subjects [49, 50, 51]. This contrasts to the traditional "spatial" FC, which is calculated using the Pearson correlation for pairs of BOLD signals, but does not involve time lags.

Initially, we use the binarized average SC matrix described in the previous section for all subjects to determine which intracortical connections exist in the model (i.e., the EC topology). This reduces the number of parameters, improving the robustness of the estimation. As detailed below, the EC weights come from the optimization of the model to reproduce the spatio-temporal structure of the BOLD signals, which is simply the covariances without and with a time lag equal to 1 TR (temporal resolution of the BOLD measurements). This contrast to previous studies that used SC values for the connectivity weights in their model, while tuning local dynamics such as Kuramoto oscillators or mean-field approximation of spiking neurons [52, 53, 13]. Our estimation procedure can be seen as a "projection" of the empirical spatio-temporal BOLD structure on the space of model parameters. Importantly, the individual values of the estimated EC weights do not depend on SC values, but are determined by the optimization procedure that strive for the model FC to best reproduce the empirical FC. It is also worth noting that EC is a directed and weighted matrix.

Now we recall details about the MOU process that will be useful for the calculation of our graph-like measures. The MOU process is determined by (i) a local leakage, (ii) a directed weighted graph associated with linear coupling and (iii) fluctuating inputs with zero mean and given covariances. In matrix form it reads

$$\mathrm{d}\mathbf{x} = J\mathbf{x}\mathrm{d}t + \mathrm{d}\zeta, \tag{1}$$

where the Jacobian matrix J is determined by the decay time constant τ (identical for all ROIs) and A_{ij} is the EC weight from ROI j to ROI i (different from the usual convention in graph theory):

$$J_{ij} = -\frac{\delta_{ij}}{\tau} + A_{ij}; \tag{2}$$

here δ_{ij} is the Kronecker delta (equal to 1 when $i = j$ and 0 otherwise). Similar to a transition matrix for a Markov chain, the whole-brain EC determines the Jacobian of the dynamic system. Last, the fluctuating input to ROI i is denoted by ζ_i is a Wiener process (temporally white noise). The covariance matrix of all ζ_i is denoted by Σ. To ensure stable dynamics, the local leakage determined by τ corresponds to a Jacobian J whose eigenvalues have strictly negative real part. In particular, the dominating eigenvalue (or spectral diameter) of the weight matrix A needs to satisfy $\lambda_{\max} < -1/\tau$.

In practice, the topology of the network (where absent connections correspond to zero EC weights) determined by SC defines a sparse EC matrix [14]. For each fMRI session, we calculate τ from the BOLD autocovariances, then estimate A and Σ. To do so, each of the A_{ij} for existing connections and Σ_{ii} are iteratively optimized to reproduce the covariances of fMRI signals involving time shifts (empirical FC matrices). Here we constrain Σ to be diagonal (although it may involve cross-covariances in addition to variances in general). The corresponding Lyapunov optimization is detailed in previous papers [14, 32]. Note that we use simplified notation for compactness here, as compared to those previous publications.

2.3. Communicability and flow to measure interactions between ROIs across time

Following our previous paper [34], we firstly define "dynamic" *communicability* to characterize the network interactions due to the connectivity A, ignoring the input properties Σ. Our definition is adapted to study complex networks associated with realistic (stable) dynamics where time has a natural and concrete meaning. In comparison, a previous version of communicability for graphs [6] relied on abstract dynamics. The basis of our framework is the network response over time, or Green function, which is the basis of the concept of dynamic communicability, which focuses on the temporal evolution of such interactions. Although we constrain the present study to the MOU process, our framework can be easily adapted to distinct local dynamics for which the Green function is known. In addition to the EC matrix A, the MOU dynamics is determined by the input properties. Here communicability is the "deformation" of the Green function e^{Jt} of the MOU process due to the presence of the (weighted and directed) matrix A, as compared to the Green function $e^{J^0 t}$ corresponding to the Jacobian with leakage only and no connectivity, $J_{ij}^0 = -\delta_{ij}/\tau$. It is defined as the family of time-dependent matrices depicted in Fig. 1a:

$$\mathcal{C}(t) = ||J^0||\left(e^{Jt} - e^{J^0 t}\right) . \tag{3}$$

The scaling factor $||J^0||^{-1} = ||\int_{t \geq 0} e^{J^0 t} dt||$ where $||\cdot||$ is the L1-norm for matrices (i.e., sum of elements in absolute value) is used for normalization purpose [34]. Recall that $t \geq 0$ here is the time for the propagation of activity in the network, referred to as 'impulse-response time' in the figures.

From the time-dependent matrices $\mathcal{C}(t)$, we define the total communicability that sums all interactions

$$\mathcal{S}^{\mathcal{C}}(t) = \sum_{\{i,j\}} \mathcal{C}_{ij}(t) . \tag{4}$$

Total communicability for graphs has been used to define a type of centrality that measures how "well-connected" nodes are [8] and corresponds here to how much activity they exchange. We also define the diversity (or heterogeneity) among the ROI interactions in the time-dependent matrices $\mathcal{C}(t)$, which can be seen as a proxy for their homogenization over time:

$$\mathcal{D}^{\mathcal{C}}(t) = \frac{\sigma_{\{i,j\}}[\mathcal{C}_{ij}(t)]}{\mu_{\{i,j\}}[\mathcal{C}_{ij}(t)]} , \tag{5}$$

defined as a coefficient of variation where $\mu_{\{i,j\}}$ and $\sigma_{\{i,j\}}$ are the mean and standard deviation over the matrix elements indexed by (i, j).

To incorporate the effect of local spontaneous activity or excitability (inputs in the model), we define the flow that fully characterizes the complex network dynamics [34]. The input statistics of interest for a stable MOU process correspond to the input (co)variance matrix Σ, which are independent parameters from the EC matrix A. This is represented by the purple arrows with various thicknesses in Fig. 1a, indicating that the ROIs may receive inputs with various levels of fluctuations. The Σ matrix may be non-diagonal when ROIs experience cross-correlated noise [32], as represented by the purple dashed arrows. The flow describes the propagation of local fluctuating activity over time via the recurrent connectivity and is defined by the

$$\mathcal{F}(t) = \mathcal{C}(t)\sqrt{\Sigma} , \tag{6}$$

where $\sqrt{\Sigma}$ is the real symmetric "square-root" matrix of the input covariance matrix, satisfying $\Sigma = \sqrt{\Sigma}\sqrt{\Sigma}^{\dagger}$. Communicability is thus a particular case of the flow for homogeneous input statistics. Similar expressions to Eqs. (4) and (5) are used to define $\mathcal{S}^{\mathcal{F}}(t)$ and $\mathcal{D}^{\mathcal{F}}(t)$ for the flow matrices $\mathcal{F}(t)$.

2.4. Community detection

To detect communities from $\mathcal{C}(t)$ or $\mathcal{F}(t)$, we rely on Newman's greedy algorithm for modularity [54] that was originally designed for weight-based communities in a graph. Adapting

6

it here to the flow matrix $\mathcal{F}(t)$ at a given time t, we seek for communities where ROIs have strong bidirectional flow interactions. In the same manner as with weighted modularity, we calculate a null model for EC:

$$A^{\mathrm{null}} = \frac{\mathbf{a}^{\mathrm{in}}\mathbf{a}^{\mathrm{out}\,\dagger}}{\mathcal{S}^A}\ . \tag{7}$$

Note that we preserve the empty diagonal. The resulting matrix contains from the expected weight for each connection, given the observed input strengths $\mathbf{a}^{\mathrm{in}}$ and output strengths $\mathbf{a}^{\mathrm{out}}$; $\mathcal{S}^A$ is the total sum of the weights in A. Then we caclulate $\mathcal{F}^{\mathrm{null}}(t)$ using Eq. (6) with A^{null} instead of A. Starting from a partition where each ROI is a singleton community, the algorithm iteratively aggregates ROIs to form a partition of K communities denoted by S_k that maximizes the following quality function:

$$\Phi = \sum_{1 \leq k \leq K} \sum_{i,j \in S_k} \left(\mathcal{F}(t) - \mathcal{F}^{\mathrm{null}}(t) \right)_{ij} + \left(\mathcal{F}(t) - \mathcal{F}^{\mathrm{null}}(t) \right)_{ji}. \tag{8}$$

At each step of the greedy algorithm, the merging of two of the current communities that maximizes the increase of Φ is performed. Communicability-based communities are defined similarly using $\mathcal{C}(t)$ and the corresponding null model $\mathcal{C}^{\mathrm{null}}(t)$.

## 3. Quantification of brain communication evaluated from fMRI data

This section applies the presented framework to fMRI data (see Fig. 1a). We use the model estimates obtained from 77 subjects recorded during 8 minutes at rest with eyes closed in a scanner and the python code available on `github.com/MatthieuGilson/WBLEC_toolbox`). In this study we present results on averages over subjects, leaving individual discrepancies for future work. We firstly show how communicability provides information about the topology of the estimated EC (leaving out the estimated input variances Σ), from the global level of the whole network to the local level of individual connections or ROIs, including the detection of communities of ROIs. Finally, we take into account the estimated inputs related to Σ (in purple in the right diagram of Fig. 1a) and analyze the flow. (Note that communicability is a particular case of the flow when inputs are homogeneous, which will be discussed later.)

3.1. Communicability provides both global and local information about the brain network

In the present formalism, communicability is the family of matrices $\mathcal{C}(t)$ in Fig. 1b that describe the interactions between pairs of ROIs across time, as the response to a standard perturbation occurring at the source ROI at time $t = 0$. In essence, each directed matrix measures how a fluctuation applied at a source ROI propagates throughout the network via the recurrent EC and impacts the target ROI later in time. The corresponding lag is referred to as 'impulse-response time' t. The theory is based on the Green function or impulse response of the network, see Eq. (3) in Methods. This directed measure thus integrates all possible pathways between the source and target ROIs, while taking the nodal dynamics of the model into account (here a exponential decay related to a time constant τ, see Fig. 1a).

Initially aligned with EC (i.e., interactions through the strong direct connections dominate), the pattern of communicability progressively reshapes and the superiority of strong EC weights dilutes, as illustrated in Fig. 1c. In particular, unconnected regions may have strong communicability due to network effects (see crosses for EC = 0 on the left of the plots). This homogenization results from the superposed loops in the EC matrix that generate a strong overall feedback that distributes the effect of the fluctuation.

The strong network feedback is further illustrated by the total dynamic communicability $\mathcal{S}^{\mathcal{C}}$ in the top panel of Fig. 1d raises to reach a maximum around 12 TR, before decaying very slowly. The homogenization is reflected in the communicability diversity $\mathcal{D}^{\mathcal{C}}$ (bottom panel) that quickly decays to stabilize after 20 TR. Note that, meanwhile, the $\mathcal{S}^{\mathcal{C}}$ is still high. This curves provide a signature for the estimated EC, which can be analyzed to uncover its topological properties.

7
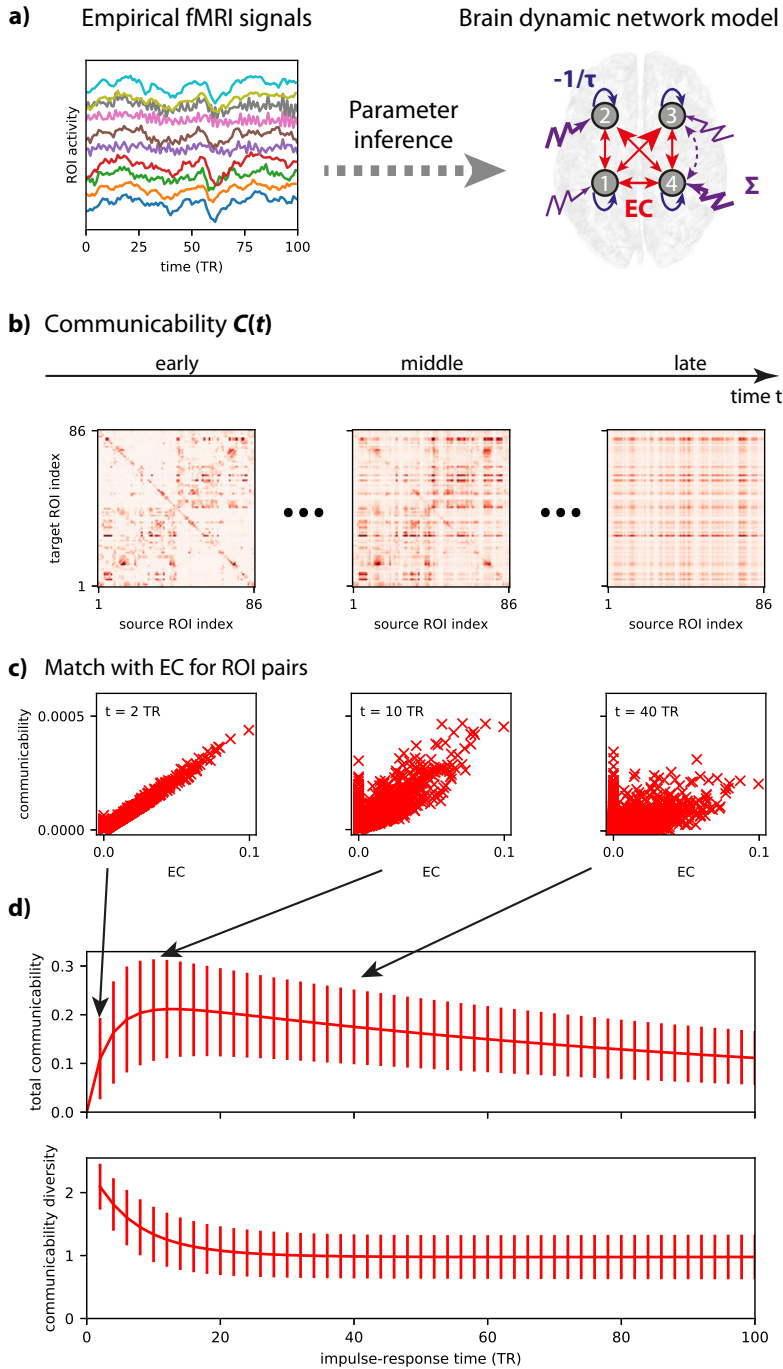
Fig. 1: **Whole-brain communicability evaluated from fMRI signals. a)** From the fMRI signals (left plot), these parameters for a dynamic system are estimated (right diagram). The network parameters comprise of the EC matrix A (red arrows) and self-inhibition corresponding to the time constant τ (blue arrows), see Eq. (2). Note that not all possible connections exist in the network, whose topology is determined by anatomical SC. In addition, the local excitabilities or inputs (purple arrows) are determined by their covariance matrix Σ. Here only 4 ROIs are represented for readability. Details about the dynamic model and estimation procedure can be found in previous studies [14]. **b)** Communicability for a single subject, corresponding to the family of matrices $\mathcal{C}(t)$ in Eq. (3) that involves the exponential of the Jacobian multiplied by time $t \geq 0$. Recall that t corresponds to the integration time for fluctuating activity in the network. Communicability is a particular case of the flow where input statistics are ignored. **c)** Match between EC and communicability for each pair of ROIs (red crosses) at three times for the same subject as in panel **b**. **d)** Total communicability $\mathcal{S}^{\mathcal{C}}$ defined as in Eq. (4) that measures the overall network feedback. The x-axis represents the impulse-response time in units of the scanner measurements (time resolution, or TR, equal to 2 s). The curves correspond to the average over the 77 subjects and the error bars the standard deviation. Diversity of communicability $\mathcal{D}^{\mathcal{C}}$ defined as in Eq. (5) that quantifies the homogenization of interactions across time.

8
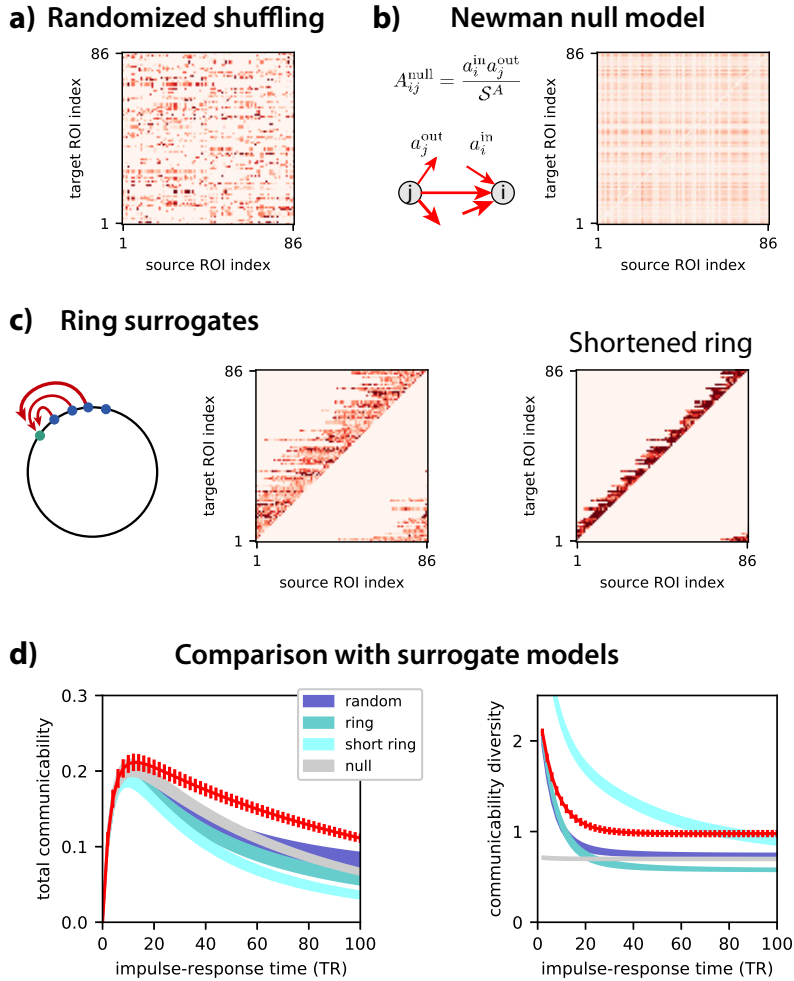
Fig. 2: **Comparison of the estimated model with surrogates. a)** Randomized version of the estimated EC matrix A (similar to the left panel in Fig. 1b) by globally shuffling the target ROIs. **b)** The null-model connectivity is calculated using Eq. (7) redistributes the weights while preserving the input and output strengths for each ROI. This results in a full matrix, apart from the empty diagonal. **c)** The ring surrogates consider the initial ROI order and reallocate the non-zero weights in the original A to the preceding ROIs. The ring preserves the number of connections (hence the density), whereas the shortened ring corresponds to grouping connections three by three, resulting in fewer connections. **d)** The total communicability $\mathcal{S}^{\mathcal{C}}$ and the corresponding diversity $\mathcal{D}^{\mathcal{C}}$ in red are the same as in Fig. 1d, but the error bars indicate the standard error of the mean here (much smaller than the standard deviation). The colored areas correspond to the surrogate networks in **a** to **c**, which preserve part of the connectivity statistics of the original A (see Table 2). The transformations being applied individually for each subject. The variability of the curves (represented by the thickness of the plotted area) corresponds to the standard error of the means over subjects, as error bars for the red curve.

Table 2: This table shows which properties of the original network are preserved (✓) or randomized (✗) by the surrogates.

Property	random	null	ring	short ring
Mean weight	✓	✓	✓	✓
In weight for each ROI	✗	✓	✓	✓
Out weight for each ROI	✗	✓	✗	✗
Density	✓	✗	✓	✗

3.2. Comparison with reference networks

Communicability enables the quantitative comparison of the estimate for brain dynamics with other reference network models. Here we compare the global measures of total communicability $\mathcal{S}^{\mathcal{C}}$ and its diversity $\mathcal{D}^{\mathcal{C}}$ in Fig. 1d to their counterparts for surrogate networks obtained by manipulating the EC estimates. The comparison between the timescales associated with the corresponding curves provides insight about equivalent topologies to generate dynamics similar to the model estimates. Topological properties such as strong feedback and short path length are reflected in $\mathcal{S}^{\mathcal{C}}$ and $\mathcal{D}^{\mathcal{C}}$ [34].

In Fig. 2d, the evolution of $\mathcal{S}^{\mathcal{C}}$ and $\mathcal{D}^{\mathcal{C}}$ for the original data (red curves) is compared with four surrogate models:

- The random surrogate in Fig. 2a reallocates the weights to a pair of ROIs. The exact weight distribution is conserved in the network, but not for each ROIs.

- The null model in Fig. 2b was proposed for Newman modularity [54] to detect communities and corresponds to resulting a full matrix with for each pair of ROIs the expected weight that preserves the distribution of input and output strengths over each ROI, see Eq. (7) for details.

- The ring surrogate in Fig. 2c (left matrix) reorganizes the input connections for each ROI to promote local connectivity with a ring topology determined by the index of the ROIs. In this arbitrary topology, distant ROIs are not directly connected.

- The shortened ring in Fig. 2c (right matrix) is similar to the previous ring surrogate, but with pooling every 3 input connections, resulting in lower density (by a factor 3).

In each case, the shuffling of the original estimate is performed for each subject and the average over subjects is then calculated. Importantly, these surrogates all destroy parts of the statistics of the original weight distribution in the estimated A in a specific manner while preserving others. They all preserve the total weight in A, which is the 1st-order moment of the weight distribution, and leave the diagonal empty. For example, the random and ring surrogates both preserve the connectivity density (1st-order of the overall distribution for the binarized weight matrix) as they topologically reallocate weights from connection to connection in a one-by-one mapping, but only the ring surrogate preserves the original sum of input weights for each ROI. This is summarized in Table 2, where the mean input and output weight per ROI, which is the first order of the weight distribution "projected" in one dimension of the weight matrix. Note that each surrogate also destroys the second-order statistics, corresponding to the joint distribution of weights for pairs of ROIs.

The random surrogate (dark blue curve) exhibits a smaller values for $\mathcal{S}^{\mathcal{C}}$ and a homogenization slightly after 20 TR, but at a lower asymptotic value for $\mathcal{D}^{\mathcal{C}}$. The ring surrogate (dark cyan curve) destroys the local loops and clusters, which decreases $\mathcal{S}^{\mathcal{C}}$ even more strongly than for the random surrogate. In our previous theoretical study, we used ring lattice to study how communicability captures the small-worldness in networks, which corresponds to a quick stabilization of $\mathcal{D}^{\mathcal{C}}$ compared to the timescale of $\mathcal{S}^{\mathcal{C}}$ [34, Fig. 6]. Here the estimated EC exhibits a profile for $\mathcal{D}^{\mathcal{C}}$ that is much closer to the random surrogate than the ring lattice, indicating that the fluctuating activity quickly propagates throughout the whole network.

Because both surrogates have the same density and individual weights, this suggests a specific internal organization for the estimated EC, related to the multiple loops and resulting in a strong network effect. A possible explanation is the existence of modules [34, Fig. 7], which will be further studied later using community detection.

For the short ring surrogate (light cyan curve), the main difference concerns the much slower homogenization for $\mathcal{D}^{\mathcal{C}}$. This arises because shortest paths between ROIs are much longer for the short ring (light cyan curve) than the ring surrogate (dark cyan curve). This shows that the mean weight per ROI is not the relevant feature to understand the propagation of activity in the network.

Last, the null model (gray curve) also has a weaker $\mathcal{S}^{\mathcal{C}}$, but more interesting is the flat curve for $\mathcal{D}^{\mathcal{C}}$. This illustrates the already-homogenized (fully-connected) network for the surrogate obtained by randomizing the second order statistics of the connectivity. This point will become important when performing community detection based on communicability or flow. The comparison of those descriptors for the estimated EC with the surrogates —each specifically destroying part of the weight structure— gives insight about how close or distant the brain network dynamics are with respect to the corresponding stereotypical models.

### 3.3. ROI-specific analysis and comparison with SC and FC

The brain network structure determines a hierarchy among ROIs. For binary graphs, the notions of degree and centrality have been used to detect highly connected ROIs, or hubs. This type of approach has been used to explore the importance of ROIs in the brain based on SC or FC data [56, 1]. A limitation of this approach is that SC and FC do not have directional information (i.e., they are symmetric matrices). Graph communicability [7] can be used to describe differentiated input and output properties for the ROIs. We now show how our dynamic communicability can be used to characterize ROIs in the network and over time.

The overall picture obtained from EC is differentiated roles for the ROIs, with listeners and broadcasters (or both), as indicated by the input and output communicability in Fig. 3a. This relates to the propagation nature of fMRI signals, which is related to the asymmetry of estimated EC matrices [14] and is in line with previous results of the fMRI lag structure [51]. Compared to our previous analyses focused on individual EC connections [32, 57], communicability provides a description of the ROI role over time. Interestingly, each ROI has its own amplitude and timescale that incorporates network effects —as illustrated in Fig. 3b and c— and it may be distinct for input and output. ROIs usually classified as hubs such as the precuneus (PCUN) and superior frontal cortex (SF) exhibit strong input communicability, which classifies it as a listening ROI, integrating the activity from other ROIs. In comparison, the superior parietal cortex (SPAR) has more balanced input and output communicabilities.

To further interpret these results, Fig. 3d compares the input and output communicability of each ROI (measured at the peak at $t = 14$ TR) to their counterparts with SC and FC. We find that output communicability strikingly differs from SC/FC degrees and strengths (triangles in the right plots). In contrast, input communicability appear to be strongly correlated with SC/FC (dots in the left plots). Evaluating the statistical (in)dependence between these ROI values, we find an explained variance of R^2 (evaluated for each subject, then averaged over them) of 31% between input communicability and the SC degree. Likewise, we find 22% between the output FC strength and the output communicability (even though the relationship for the average over subjects in Fig. 3d is less obvious). It is less than 10% otherwise. It appears that regions with strong input communicability have sufficiently many connections to support it, on average. It was previously shown that EC weights are modulated in a task-dependent manner [32, 57]. In particular, the output EC weights of ROI hubs are down-regulated at rest as compared to visual tasks [57]. This suggests that not all existing EC pathways are used at rest, which may explain the very weak correlation of output communicability with SC in Fig. 3. In conclusion, our model-based approach provides distinct information from the classical analyses based on SC/FC alone.

11
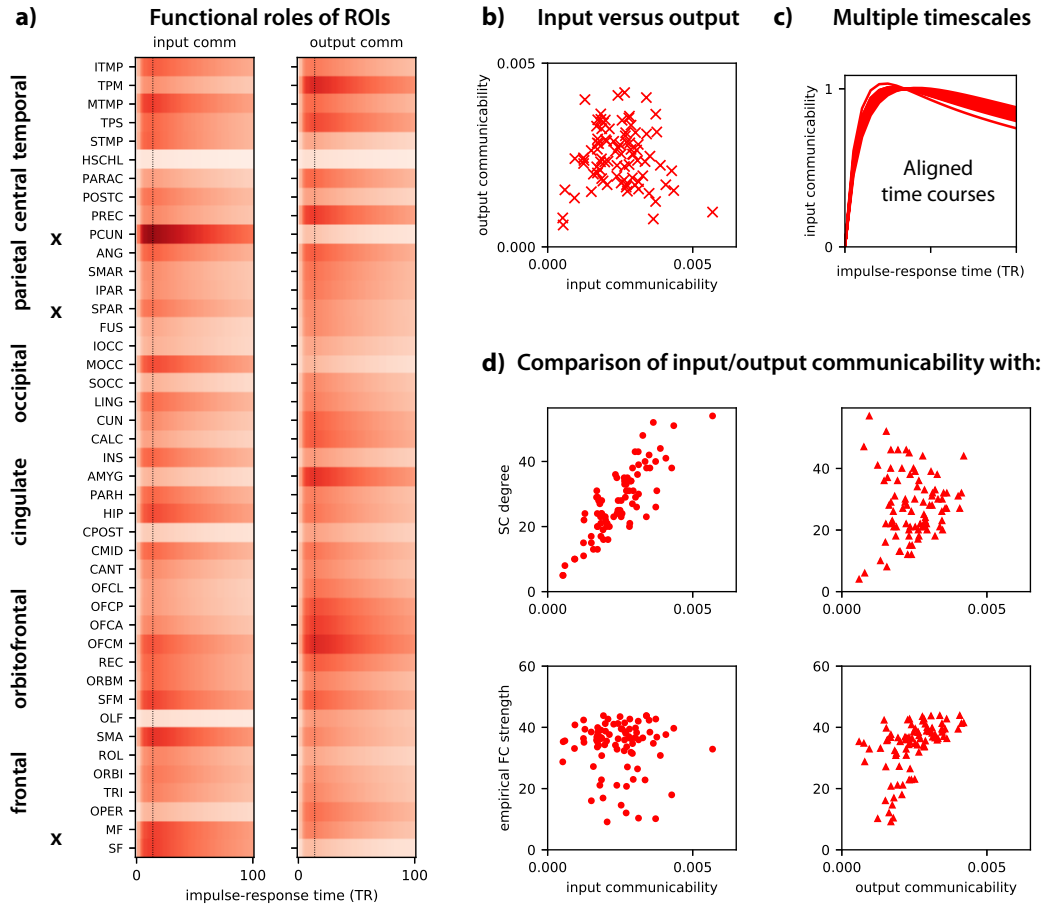
Fig. 3: **Characterization of ROI roles and comparison with information obtained from SC and FC. a)** Temporal evolution of input and output communicability for all ROIs. The values are averages over the two hemispheres and all subjects. The ROIs are grouped by anatomical areas and black crosses indicate the three ROIs that are mentioned in the main text. **b)** Comparison of input and output communicability for each ROI (red cross). The plotted value is taken at the maximum $t = 14$ TR, indicated by the dashed vertical lines in **a**. **c)** The superposed time courses for input communicability reveals heterogeneous timescales across the ROIs. **d)** Comparison of the input and output communicability (left and right panels in each row with dots and triangles, resp.) with the SC degrees and empirical FC strengths. Each symbol represents the value for a ROI, averaged over all subjects; for communicability, it is taken at the time corresponding to the dashed vertical lines in **a**.
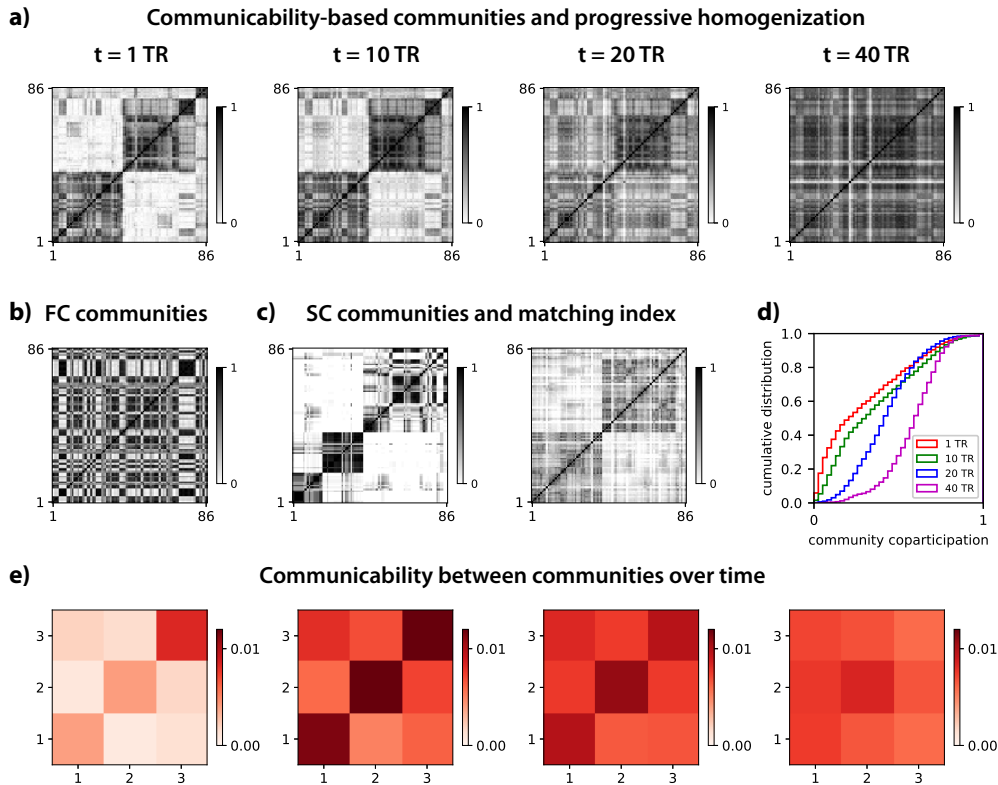
Fig. 4: **Communicability-based communities and homogenization of cortical activity.** **a)** Each matrix represents the communities of cortical regions with strong communicability for four values of t. Regions are paired when they have strong bidirectional communicability between them, see Eq. (8) for details. They correspond to averages over the 77 subjects and darker pixels indicate that the two regions (on the x- and y-axis) belong to the same community over all subjects. The region ordering is the same for all plots. **b)** Similar plots to **a** with the FC-based communities. **c)** Similar plot (left panel) to **a** for SC-based communities obtained with the individual matrix with DWI values, see Methods. The right panel display the matrix of matching indices for SC, which measures the overlap between connected targets for each pair of ROIs. **d)** Cumulative distribution of the community coparticipation values in **a** for the 4 matrices. **e)** The matrices indicate the average communicability between the three communities obtained at $t = 1$ TR in **a**.

13

3.4. Functional communities in brain network and information integration

The high saturating value of $\mathcal{D}^{\mathcal{C}}$ in Fig. 1d is also reminiscent of hierarchical networks consisting of several modules that have rather strong coupling between them, for which the diversity stabilizes early when the total communicability is still large and close to its peak [34, see Fig. 7 there]. To further examine this aspect, we perform a community analysis to reveal the communication between ROI groups over time. In essence, communicability is compared to that obtained with the null connectivity model in gray in Fig. 2. ROIs with greater reciprocal communicability compared to the null model are grouped into communities, yielding the coparticipation matrices in Fig. 4a. These matrices measure the robustness of the communities across subjects: Well-defined correspond to dark squares on the diagonal (after reordering the ROIs), whereas weak associations of ROIs appear in lighter gray. Note that the ordering of the brain regions corresponds to the 3 communities obtained at $t = 1$ TR: From the lower left to the upper right, the two largest communities correspond to the two hemispheres, while the third and smallest comprises of the bilateral precuneus and cingulate ROIs (PCUN, CANT, CMID and CPOST in Table 1).

We firstly compare these four community matrices with the same algorithm applied on FC and SC, as classically performed. The resulting community matrices in Fig. 4b and c (left panel) are distinct from those obtained from communicability in several aspects. FC-based communities are less evident (with darker pixels on average), suggesting that even the strong overall correlations between regions do not adequately determine the functional communities. This comes partly from the fact that FC is a full matrix. SC-based communities (averaged over subjects) are clearly defined and correspond to at least 5 groups, where the two hemispheres appear to be each divided in two groups. The right matrix in Fig. 4c displays the pairwise matching indices calculated for the (binarized) SC. The matching index [58] quantifies the fraction of common neighbors two ROIs share and is thus often considered as a measure of "functional similarity". Since the matching index is based on first-neighbor interactions, we find that this simplified estimate based on the topology alone satisfactorily predicts diffusion the propagation at early times described by communicability. Our results confirm that, although the communicability structure is correlated with FC and SC to some extent at the ROI level in Fig. 3, the discrepancies at the connection level involve a different organization.

Another advantage of our approach is the quantitative description of the community merging over time, as illustrated by the distributions of coparticipation indices in Fig. 4d. The communities remain distinct for $t \leq 10$ TR in Fig. 4a, but the difference vanishes for $t \geq 20$ TR. The average communicability between the communities in Fig. 4e confirms this global pattern: It suggests that information is first integrated somehow independently within distinct communities, then is broadcasted to the whole network during the homogenization phase. These two modes of information integration are reminiscent of synchronization in networks for distinct values of the global coupling [59, 60], but it is important to note that they are supported by the same dynamic regime in our case; they simply occur at different timescales within the network response.

3.5. Importance of heterogeneities in local excitability for functional communities

So far, we have analyzed the communicability that depends on the connectivity only. However, the model-based estimation tunes the local excitability for each ROI (input variances in the model, see Fig. 1a) in addition to the network connectivity. The Σ estimates have been shown to be modulated when engaging a task, such as movie viewing as compared to rest [32]. Now we incorporate these excitabilities in the community analysis using the flow to examine whether they provide additional information as compared to the connectivity alone for resting-state fMRI. Fig. 5a displays the flow-based communities, which differ from the communicability-based ones in spite of the correlation between the flow and communicability (Fig. 5b for a single subject). This illustrates the importance of taking into account all the model parameters that determine the system dynamics, here the input variances Σ in addition to EC. Nonetheless, the global homogenization process is similar to communicability-based communities (Fig. 5c).
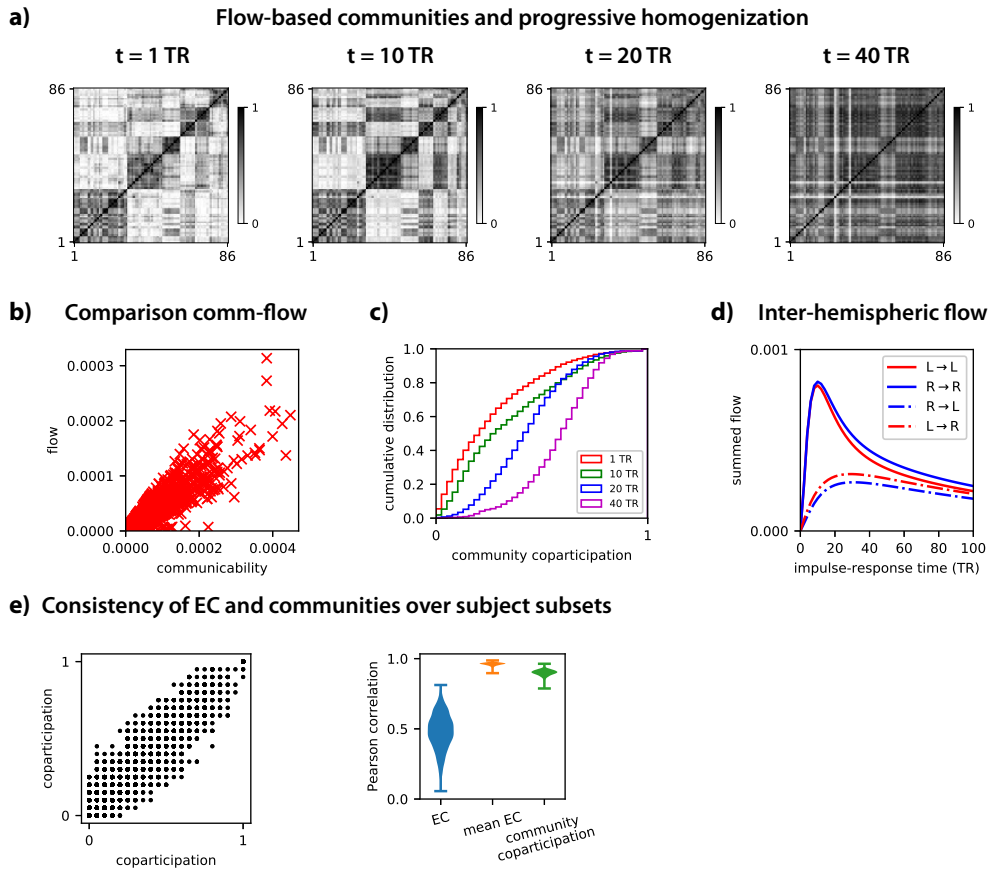
a)   **Flow-based communities and progressive homogenization**

b)   **Comparison comm-flow**   **c)**   **d)**   **Inter-hemispheric flow**

e)   **Consistency of EC and communities over subject subsets**

Fig. 5: **Flow-based communities. a)** Flow-based communities at the four times, similar to Fig. 4a. Note that the ROI ordering differs from Fig. 4. **b)** Comparison between communicability and flow matrix elements for a single subject (at the maximum $t = 12$ TR). **c)** Histograms of community coparticipation values, similar to Fig. 4b. **d)** Comparison between the within- and between-hemisphere flow over time. L and R indicate the left and right hemispheres, respectively. **e)** Stability of EC and community detection for 100 repetitions using randomly 25% of the 77 subjects. The left plot represents the alignment of the communities for two subsets of subjects (matrix elements in panel **a** for $t = 1$ TR). The right plot displays the Pearson correlation coefficient between the EC of the 77 subjects, between the mean EC over each subject subset and of the community coparticipation values.

Previous work [61] showed asymmetries in the left and right within-hemisphere FC patterns. In our data we observe to some degree discrepancies between the two hemispheres in the flow-based communities in Fig. 5a, as well as in the communicability-based communities in Fig. 4a. In addition, Fig. 5d shows that the flow is initially much higher within each hemisphere (solid curves) than between hemispheres (dashed curves), but eventually reaches similar values around 50 TR. This points to weaker inter-hemispheric communication compared to within-hemispheric communication at rest. Our previous results based on EC indicated stronger inter-hemispheric communication when analyzing changes of individual EC weights when engaging a passive-visual task [32], which would be interesting to quantify at the network level using the present formalism.

Finally, we verify the robustness of the community detection by performing the same procedure with subsets of 25% of the 77 subjects. The left plot of Fig. 5e shows the correspondence between coparticipation values (matrix elements in Fig. 5a) for two subsets. From this we calculate the Pearson correlation coefficient to evaluate the alignment of the communities, which corresponds to 0.9 (green distribution in the right of Fig. 5e). This comes because the mean EC over the subjects in each subset have a very similar structure (orange distribution), even though individual EC are more moderately aligned (blue distribution).

4. Discussion

The present paper has introduced a network-oriented analysis of effective connectivity (EC) obtained from fMRI data, applying our recently-proposed formalism [34]. It demonstrates the flexibility of the framework that provides information at both local (single connections or ROIs) and global levels, allowing for a comprehensive description of the network going beyond a link-specific analysis. The pairwise interactions across time determined by the network dynamics are described by a family of matrices that incorporate network effects. Our results stress the importance of taking time into account to describe the brain communication in order to describe how "information" —here measured via the propagation of BOLD signals— is integrated in the network. Variability across subjects has not been explored here, but is of interest and will be studied in future work.

The BOLD signals obtained from fMRI are "projected" on the model parameters. EC acts as a transition matrix, measuring the propagation of fMRI (fluctuating) activity across brain areas. In addition, the input properties are described via their (co)variance matrix Σ. In our model-based approach, the network analysis thus characterizes the brain *dynamics*, whose consistency from estimation to interpretation is a strength compared to previous studies in our opinion. As an example, FC-based analysis can be considered as a "projection" of BOLD signals on a graphical model, where the successive levels of BOLD activation (for all ROIs) are considered as i.i.d. variables over time. Likewise, sliding-window FC measures are typically considered as a pool of measures with no intrinsic temporal structure [18, 19, 20], which has also been used in other fields such as epidemic spreading [62]. Another model-free alternative to define states and transitions between them has used clustering techniques on the instantaneous phases obtained from the Hilbert transform [63]. Although these approaches have proven useful to describe time-dependent interactions between ROIs, they do not capture the propagation nature of the BOLD signals. In addition, our approach conceptually differs from previous network studies that applied various types of nodal dynamics —such as Kuramoto oscillators and noise-diffusion processes— to static networks in order to reveal the properties of their complex topologies [35, 36, 37]. This formalism thus opens a new dynamical perspective to interpret fMRI data, as compared to more "static" approaches using network theory that focused on FC or SC [2, 1].

In our framework two families of time-dependent matrices are defined to analyze the brain dynamics. *(Dynamic) communicability* accounts for the estimated EC alone, while the *flow* also incorporates the effect of the estimated input properties (covariances Σ). In fact, communicability is a particular case of the flow when inputs are homogeneous (Σ is the identity matrix). As illustrated by the comparison between Fig. 4 and 5, functional communities evaluated from the brain dynamics do not only depend on the estimated EC,

but also on the heterogeneities in Σ. In practice, the difference between the two measure is the following: Communicability describes how standard input fluctuations propagate throughout the estimated EC, whereas the flow quantifies the propagation of fluctuating activity for the estimated brain dynamical "state". Communicability is thus appropriate to study the propagation of perturbations in the network, whereas the flow is better suited when Σ depends on the subject's condition as was shown for movie viewing versus rest [32].

The presented framework allows for the analysis of connectivity at various scales. At the global level, the total flow $\mathcal{S}^{\mathcal{F}}$ measures how the inputs circulate over time via EC. The stabilization of $\mathcal{D}^{\mathcal{F}}$ indicates the temporal horizon when the network interactions homogenize the inputs. At the local scale, we have explored the functional roles of ROIs over time, e.g., feeders or receivers (Fig. 3a), which provides complementary information to FC and SC (Fig. 3d). For instance, we have found that anatomical ROI hubs [56] are not necessarily those with larger output communicability values for the resting state. Last, community detection uncovers the functional organization of ROIs at an intermediate level (Fig. 4a-d). For the studied dataset, EC determines functional communities in a much more accurate manner than FC (Fig. 4b), at the same level as SC (Fig. 4c). This is an important point to analyze task-dependent communities, which is not possible using SC. Our results also show a multistage integration of information supported by the cortical network —first locally within the communities, then globally. These two modes emerge as a natural consequence of the timescale separation due to information propagation within the network. In contrast, previous studies could only identify such modes by "artificially" setting the network into two very different dynamical states: either weakly or strongly synchronized [59, 60]. This flexibility may be interesting to quantify the notion of integration in networks that has attracted a lot of attention, in particular in neuroscience [25, 64, 24, 30, 28].

Another interesting aspect of our formalism is the quantitative comparison with surrogate networks —such as ring lattices or random networks— in order to reveal the properties of the estimated EC. Here we have compared global measures: the total flow $\mathcal{S}$ is the sum of all interactions at a given time and the flow diversity $\mathcal{D}$ reflects their heterogeneity within the network. These time-dependent measures correspond to curves that are more or less distant, providing a metric to compare the data with specific topologies (Fig. 2).

The present analysis of the brain dynamics relies on the MOU process for both estimation and network-oriented interpretation. The multivariate measures (communicability and flow) can be derived for other dynamic system provided the Green function is known. The MOU network corresponds to a non-conservative and stable propagation of fluctuating activity, which was used to study network complexity [25, 26, 27, 28]. The MOU process has also been used in many other scientific disciplines [65, 66, 67], in particular for time-series analysis [68]. The viewpoint taken on the MOU process is a "noise"-diffusion network where fluctuating activity propagates, EC defining the input-output mapping [69].

Recall that the present interpretation of BOLD in term of brain communication relies on the assumption that changes in neural activity are reflected in the BOLD dynamics, which is under debate [70, 71, 72]. In a sense, the dynamic model to estimate our version of EC can be thought as a linearization of more elaborate models such as the dynamic causal model (DCM) that explicitly incorporates hemodynamics [33, 73]. We nonetheless stress that the MOU estimation properly deals with the subsampling related to the discrete observations of BOLD signals [14], in contrast to estimation relying on the multivariate autoregressive process. Our approach can thus be seen as an alternative to DCM that aims to solve the trade-off between robust estimation and application to large brain network (hundreds of ROIs) by using linear dynamics, as was done recently with DCM for resting-state fMRI [74, 73].

Acknowledgements

References

[1] O. Sporns, Making sense of brain network data, Nat Methods 10 (2013) 491–493.

[2] O. Sporns, G. Tononi, G. M. Edelman, Theoretical neuroanatomy: relating anatomical and functional connectivity in graphs and cortical connection matrices, Cereb Cortex 10 (2000) 127–141.

[3] R. Albert, A.-L. Barabási, Statistical mechanics of complex networks, Rev. Mod. Phys. 74 (2002) 47–97. doi:10.1103/RevModPhys.74.47.
URL https://link.aps.org/doi/10.1103/RevModPhys.74.47

[4] A. Barrat, M. Barthélemy, R. Pastor-Satorras, A. Vespignani, The architecture of complex weighted networks, Proc Natl Acad Sci U S A 101 (2004) 3747–3752. doi:10.1073/pnas.0400087101.

[5] J. Bang-Jensen, G. Gutin, Digraphs: Theory, Algorithms and Applications, 2nd Edition, Springer-Verlag, 2009.

[6] E. Estrada, N. Hatano, Communicability in complex networks, Phys Rev E Stat Nonlin Soft Matter Phys 77 (2008) 036111. doi:10.1103/PhysRevE.77.036111.

[7] E. Estrada, Communicability in temporal networks, Phys Rev E Stat Nonlin Soft Matter Phys 88 (2013) 042811. doi:10.1103/PhysRevE.88.042811.

[8] M. Benzi, C. Klymko, Total communicability as a centrality measure, Journal of Complex Networks 1 (2013) 124–149. doi:10.1093/comnet/cnt007.

[9] F. Arrigo, M. Benzi, Updating and downdating techniques for optimizing network communicability, SIAM Journal on Scientific Computing 38 (2016) B25–B49. doi:10.1137/140991923.

[10] R. G. Bettinardi, G. Deco, V. M. Karlaftis, T. J. Van Hartevelt, H. M. Fernandes, Z. Kourtzi, M. L. Kringelbach, G. Zamora-López, How structure sculpts function: Unveiling the contribution of anatomical connectivity to the brain's spontaneous correlation structure, Chaos 27 (2017) 047409. doi:10.1063/1.4980099.

[11] M. Breakspear, Dynamic models of large-scale brain activity, Nat Neurosci 20 (2017) 340–352. doi:10.1038/nn.4497.

[12] G. Deco, V. Jirsa, A. McIntosh, Emerging concepts for the dynamical organization of resting-state activity in the brain, Nat Rev Neurosci 12 (2011) 43–56.

[13] A. Messé, D. Rudrauf, H. Benali, G. Marrelec, Relating structure and function in the human brain: relative contributions of anatomy, stationary dynamics, and non-stationarities, PLoS COmput Biol 10 (2014) e1003530.

[14] M. Gilson, R. Moreno-Bote, A. Ponce-Alvarez, P. Ritter, G. Deco, Estimation of directed effective connectivity from fmri functional connectivity hints at asymmetries of cortical connectome, PLoS Comput Biol 12 (2016) e1004762.

[15] M. Schmidt, R. Bakker, C. C. Hilgetag, M. Diesmann, S. J. van Albada, Multi-scale account of the network structure of macaque visual cortex, Brain Struct Funct 223 (2018) 1409–1435. doi:10.1007/s00429-017-1554-4.

[16] S. Frässle, E. I. Lomakina, L. Kasper, Z. M. Manjaly, A. Leff, K. P. Pruessmann, J. M. Buhmann, K. E. Stephan, A generative model of whole-brain effective connectivity, Neuroimagedoi:10.1016/j.neuroimage.2018.05.058.

[17] R. M. Hutchison, T. Womelsdorf, E. A. Allen, P. A. Bandettini, V. D. Calhoun, M. Corbetta, S. Della Penna, J. H. Duyn, G. H. Glover, J. Gonzalez-Castillo, D. A. Handwerker, S. Keilholz, V. Kiviniemi, D. A. Leopold, F. de Pasquale, O. Sporns, M. Walter, C. Chang, Dynamic functional connectivity: promise, issues, and interpretations, Neuroimage 80 (2013) 360–378. doi:10.1016/j.neuroimage.2013.05.079.

[18] A. N. Khambhati, A. E. Sizemore, R. F. Betzel, D. S. Bassett, Modeling and interpreting mesoscale network dynamics, Neuroimagedoi:10.1016/j.neuroimage.2017.06.029.

[19] W. H. Thompson, P. Brantefors, P. Fransson, From static to temporal network theory: Applications to functional brain connectivity, Net Neurosci 1 (2) (2017) 69–99. doi:10.1162/NETN_a_00011.
URL https://doi.org/10.1162/NETN_a_00011

[20] A. Avena-Koenigsberger, B. Misic, O. Sporns, Communication dynamics in complex brain networks, Nat Rev Neurosci 19 (2017) 17–33. doi:10.1038/nrn.2017.149.

[21] D. Vidaurre, R. Abeysuriya, R. Becker, A. J. Quinn, F. Alfaro-Almagro, S. M. Smith, M. W. Woolrich, Discovering dynamic brain networks from big data in rest and task, Neuroimagedoi:10.1016/j.neuroimage.2017.06.077.

[22] S. F. V. Nielsen, M. N. Schmidt, K. H. Madsen, M. Mørup, Predictive assessment of models for dynamic functional connectivity, Neuroimage 171 (2018) 116–134. doi:10.1016/j.neuroimage.2017.12.084.

[23] B. Baars, A Cognitive Theory of Consciousness, Cambridge University Press, 1988.

[24] S. Dehaene, L. Naccache, Towards a cognitive neuroscience of consciousness: basic evidence and a workspace framework, Cognition 79 (2001) 1–37.

[25] G. Tononi, O. Sporns, G. M. Edelman, A measure for brain complexity: relating functional segregation and integration in the nervous system, Proc Natl Acad Sci U S A 91 (1994) 5033–5037.

[26] R. F. Galán, On how network architecture determines the dominant patterns of spontaneous neural activity, PLoS One 3 (2008) e2148. doi:10.1371/journal.pone.0002148.

[27] L. Barnett, C. L. Buckley, S. Bullock, Neural complexity and structural connectivity, Phys Rev E Stat Nonlin Soft Matter Phys 79 (2009) 051914. doi:10.1103/PhysRevE.79.051914.

[28] G. Zamora-López, Y. Chen, G. Deco, M. L. Kringelbach, C. Zhou, Functional complexity emerging from anatomical constraints in the brain: the significance of network modularity and rich-clubs, Sci Rep 6 (2016) 38424. doi:10.1038/srep38424.

[29] D. A. Fair, N. U. F. Dosenbach, J. A. Church, A. L. Cohen, S. Brahmbhatt, F. M. Miezin, D. M. Barch, M. E. Raichle, S. E. Petersen, B. L. Schlaggar, Development of distinct control networks through segregation and integration, Proc Natl Acad Sci U S A 104 (2007) 13507–13512. `doi:10.1073/pnas.0705843104`.

[30] G. Deco, G. Tononi, M. Boly, M. L. Kringelbach, Rethinking segregation and integration: contributions of whole-brain modelling, Nat Rev Neurosci 16 (2015) 430–439. `doi: 10.1038/nrn3963`.

[31] P. Fransson, B. C. Schiffler, W. H. Thompson, Brain network segregation and integration during an epoch-related working memory fmri experiment, Neuroimage 178 (2018) 147–161. `doi:10.1016/j.neuroimage.2018.05.040`.

[32] M. Gilson, G. Deco, K. Friston, P. Hagmann, D. Mantini, V. Betti, G. L. Romani, M. Corbetta, Effective connectivity inferred from fmri transition dynamics during movie viewing points to a balanced reconfiguration of cortical interactions, Neuroimage `doi: 10.1016/j.neuroimage.2017.09.061`.

[33] K. Friston, Functional and effective connectivity: A review, Brain Connect 1 (2011) 8.

[34] M. Gilson, G. Zamora-Lopez, N. E. Kouvaris, G. Deco, Dynamic communicability and flow to describe complex network dynamics with linear feedback, Phys Rev E 97 (2018) 052301.

[35] A. Arenas, A. Díaz-Guilera, C. J. Pérez-Vicente, Synchronization reveals topological scales in complex networks, Phys Rev Lett 96 (2006) 114102. `doi:10.1103/ PhysRevLett.96.114102`.

[36] S. Boccaletti, M. Ivanchenko, V. Latora, A. Pluchino, A. Rapisarda, Detecting complex network modularity by dynamical clustering, Phys Rev E Stat Nonlin Soft Matter Phys 75 (2007) 045102. `doi:10.1103/PhysRevE.75.045102`.

[37] M. Rosvall, C. T. Bergstrom, Maps of random walks on complex networks reveal community structure, Proc Natl Acad Sci U S A 105 (2008) 1118–1123. `doi:10.1073/pnas. 0706851105`.

[38] Y. Assaf, D. C. Alexander, D. K. Jones, A. Bizzi, T. E. J. Behrens, C. A. Clark, Y. Cohen, T. B. Dyrby, P. S. Huppi, T. R. Knoesche, D. Lebihan, G. J. M. Parker, C. Poupon, CONNECT consortium, D. Anaby, A. Anwander, L. Bar, D. Barazany, T. Blumenfeld-Katzir, S. De-Santis, D. Duclap, M. Figini, E. Fischi, P. Guevara, P. Hubbard, S. Hofstetter, S. Jbabdi, N. Kunz, F. Lazeyras, A. Lebois, M. G. Liptrot, H. Lundell, J.-F. Mangin, D. M. Dominguez, D. Morozov, J. Schreiber, K. Seunarine, S. Nava, C. Poupon, T. Riffert, E. Sasson, B. Schmitt, N. Shemesh, S. N. Sotiropoulos, I. Tavor, H. G. Zhang, F.-L. Zhou, The CONNECT project: Combining macro- and micro-structure, Neuroimage 80 (2013) 273–282. `doi:10.1016/j.neuroimage.2013.05.055`.

[39] D. Duclap, B. Schmitt, A. Lebois, P. Guevara, H. Zhang, C. Longo Dos Santos, D. Le Bihan, J.-F. Mangin, C. Poupon, Towards a super-resolution CONNECT/ARCHI atlas of the white matter connectivity, Proc Int Soc Magn Reson Med 21th Annual Meeting (2013) 3153.

[40] B. Fischl, M. I. Sereno, A. M. Dale, Cortical surface-based analysis. II: Inflation, flattening, and a surface-based coordinate system, Neuroimage 9 (1999) 195–207. `doi: 10.1006/nimg.1998.0396`.

[41] R. S. Desikan, F. Ségonne, B. Fischl, B. T. Quinn, B. C. Dickerson, D. Blacker, R. L. Buckner, A. M. Dale, R. P. Maguire, B. T. Hyman, M. S. Albert, R. J. Killiany, An automated labeling system for subdividing the human cerebral cortex on mri scans into gyral based regions of interest, Neuroimage 31 (2006) 968–980. `doi:10.1016/j. neuroimage.2006.01.021`.

[42] N. Tzourio-Mazoyer, B. Landeau, D. Papathanassiou, F. Crivello, O. Etard, N. Delcroix, B. Mazoyer, M. Joliot, Automated anatomical labeling of activations in spm using a macroscopic anatomical parcellation of the mni mri single-subject brain, Neuroimage 15 (2002) 273–289. doi:10.1006/nimg.2001.0978.

[43] D. Duclap, A. Lebois, B. Schmitt, O. Riff, P. Guevara, L. Marrakchi-Kacem, V. Brion, F. Poupon, J.-F. Mangin, C. Poupon, Connectomist-2.0: a novel diffusion analysis toolbox for BrainVISA, in: 29th ESMRMB, Lisbone, Portugal, 2012.

[44] M. Descoteaux, E. Angelino, S. Fitzgibbons, R. Deriche, Regularized, fast, and robust analytical Q-ball imaging, Magn Reson Med 58 (2007) 497–510. doi:10.1002/mrm.21277.

[45] P. Guevara, D. Duclap, L. Marrakchi-Kacem, D. Rivière, Y. Cointepas, C. Poupon, F.-F. Mangin, Accurate tractography propagation mask using T1-weighted data rather than FA, in: Proc. Intl. Soc. Mag. Reson. Med, Vol. 19, 2011, p. 2011.

[46] S. Lefranc, P. Roca, M. Perrot, C. Poupon, D. Le Bihan, J.-F. Mangin, D. Rivière, Groupwise connectivity-based parcellation of the whole human cortical surface using watershed-driven dimension reduction, Med Image Anal 30 (2016) 11–29. doi:10.1016/j.media.2016.01.003.

[47] L. Chang, P. Gianaros, S. Manuck, A. Krishnan, T. Wager, A sensitive and specific neural signature for picture-induced negative affect, PLoS Biol 13 (2015) e1002180.

[48] G. Deco, M. L. Kringelbach, Great expectations: using whole-brain computational connectomics for understanding neuropsychiatric disorders, Neuron 84 (2014) 892–905. doi:10.1016/j.neuron.2014.08.034.

[49] B. J. He, Scale-free properties of the functional magnetic resonance imaging signal during rest and task, J Neurosci 31 (2011) 13786–13795.

[50] P. Ciuciu, P. Abry, B. J. He, Interplay between functional connectivity and scale-free dynamics in intrinsic fMRI networks, Neuroimage 95 (2014) 248–263.

[51] A. Mitra, A. Z. Snyder, E. Tagliazucchi, H. Laufs, M. Raichle, Propagated infra-slow intrinsic brain activity reorganizes across wake and slow wave sleep, Elife 4.

[52] J. Cabral, E. Hugues, O. Sporns, G. Deco, Role of local network oscillations in resting-state functional connectivity, Neuroimage 57 (2011) 130–139.

[53] G. Deco, A. Ponce-Alvarez, D. Mantini, G. Romani, P. Hagmann, M. Corbetta, Resting-state functional connectivity emerges from structurally and dynamically shaped slow linear fluctuations, J Neurosci 33 (2013) 11239–11252.

[54] M. E. J. Newman, Modularity and community structure in networks, Proc Natl Acad Sci U S A 103 (2006) 8577–8582. doi:10.1073/pnas.0601602103.

[55] M. Newman, Networks: An Introduction, Oxford University Press, 2010.

[56] M. P. van den Heuvel, R. S. Kahn, J. Goñi, O. Sporns, High-cost, high-capacity backbone for global brain communication, Proc Natl Acad Sci U S A 109 (2012) 11372–11377. doi:10.1073/pnas.1203593109.

[57] M. Senden, N. Reuter, M. P. van den Heuvel, R. Goebel, G. Deco, M. Gilson, Task-related effective connectivity reveals that the cortical rich club gates cortex-wide communication, Hum Brain Mapp doi:10.1002/hbm.23913.

[58] S. Wasserman, K. Faust, Social Network Analysis, Cambridge University Press, Cambridge, 1994.

[59] C. Zhou, J. Kurths, Hierarchical synchronization in complex networks with heterogeneous degrees, Chaos 16 (2006) 015104. doi:10.1063/1.2150381.

[60] J. Gómez-Gardeñes, G. Zamora-López, Y. Moreno, A. Arenas, From modular to centralized organization of synchronization in functional areas of the cat cerebral cortex, PLoS One 5 (2010) e12313. doi:10.1371/journal.pone.0012313.

[61] M. Raemaekers, W. Schellekens, N. Petridou, N. F. Ramsey, Knowing left from right: asymmetric functional connectivity during resting state, Brain Struct Funct 223 (2018) 1909–1922. doi:10.1007/s00429-017-1604-y.

[62] I. Chen, M. Benzi, H. H. Chang, V. S. Hertzberg, Dynamic communicability and epidemic spread: a case study on an empirical dynamic contact network, Journal of Complex Networks 5 (2016) 274–302. doi:10.1093/comnet/cnw017.

[63] J. Cabral, D. Vidaurre, P. Marques, R. Magalhães, P. Silva Moreira, J. Miguel Soares, G. Deco, N. Sousa, M. L. Kringelbach, Cognitive performance in healthy older adults relates to spontaneous switching between states of functional connectivity during rest, Sci Rep 7 (2017) 5135. doi:10.1038/s41598-017-05425-7.

[64] G. Tononi, G. M. Edelman, O. Sporns, Complexity and coherency: integrating information in the brain, Trends Cogn Sci 2 (1998) 474–484.

[65] O. Vasicek, An equilibrium characterization of the term structure, Journal of Financial Economics 5 (1977) 177–188. doi:doi.org/10.1016/0304-405X(77)90016-2.

[66] T. Britton, P. Neal, The time to extinction for a stochastic SIS-household-epidemic model, J Math Biol 61 (2010) 763–779. doi:10.1007/s00285-009-0320-5.

[67] P. Andersson, D. Lindenstrand, A stochastic SIS epidemic with demography: initial stages and time to extinction, J Math Biol 62 (2011) 333–348. doi:10.1007/s00285-010-0336-x.

[68] H. Lütkepohl, New introduction to multiple time series analysis, Springer Science & Business Media, 2005.

[69] M. Gilson, Analysis of fmri data using noise-diffusion network models: a new covariance-coding perspective, Biological Cyberneticsdoi:10.1007/s00422-017-0741-y. URL https://doi.org/10.1007/s00422-017-0741-y

[70] J. Goense, K. Whittingstall, N. K. Logothetis, Neural and bold responses across the brain, Wiley Interdiscip Rev Cogn Sci 3 (2012) 75–86. doi:10.1002/wcs.153.

[71] T. Matsui, T. Murakami, K. Ohki, Neuronal origin of the temporal dynamics of spontaneous bold activity correlation, Cereb Cortexdoi:10.1093/cercor/bhy045.

[72] Y. He, M. Wang, X. Chen, R. Pohmann, J. R. Polimeni, K. Scheffler, B. R. Rosen, D. Kleinfeld, X. Yu, Ultra-slow single-vessel bold and cbv-based fmri spatiotemporal dynamics and their correlation with neuronal intracellular calcium signals, Neuron 97 (2018) 925–939. doi:10.1016/j.neuron.2018.01.025.

[73] S. Frässle, E. I. Lomakina, A. Razi, K. J. Friston, J. M. Buhmann, K. E. Stephan, Regression DCM for fMRI, Neuroimage 155 (2017) 406–421. doi:10.1016/j.neuroimage.2017.02.090.

[74] K. J. Friston, J. Kahan, B. Biswal, A. Razi, A DCM for resting state fMRI, Neuroimage 94 (2014) 396–407. doi:10.1016/j.neuroimage.2013.12.009.